Acta Materialia 100 (2015) 64–72

Contents lists available at ScienceDirect

Acta Materialia

journal homepage: www.elsevier.com/locate/actamat

Atomic configurations of various kinds of structural intergrowth in the polytypic M_2B-type boride precipitated in the Ni-based superalloy

X.B. Hu [a], Y.L. Zhu [a], X.H. Shao [a], H.Y. Niu [a], L.Z. Zhou [b], X.L. Ma [a,*]

[a] Shenyang National Laboratory for Materials Science, Institute of Metal Research, Chinese Academy of Sciences, Wenhua Road 72, 110016 Shenyang, China
[b] Superalloys Division, Institute of Metal Research, Chinese Academy of Sciences, Wenhua Road 72, 110016 Shenyang, China

ARTICLE INFO

Article history:
Received 19 May 2015
Revised 10 August 2015
Accepted 13 August 2015

Keywords:
Ni-based superalloy
Polytypic M_2B-type boride
Structural intergrowth
Aberration corrected transmission electron microscope
Atomic configurations

ABSTRACT

The heavily faulted M_2B-type borides precipitated in the long-term aging Ni-based superalloys with B addition are comprehensively studied at an atomic scale. By means of high angle annular dark field (HAADF) imaging technique in the aberration corrected scanning transmission electron microscope (STEM), atomic configurations of various kinds of structural intergrowth in the profoundly faulted M_2B phase are directly imaged. The polytypic M_2B phase is mainly composed of C16, C_b and C_a structural variants, in which planar defects and the resultant long period stacking order (LPSO) structure are identified. In combination of the advanced spectrometry imaging technique with density functional theory (DFT) calculations, it is proposed that the polytypic feature is attributed to the conservation of the basic polyhedron of anti-square prisms.

1. Introduction

Due to the superior overall performance, Ni-based superalloys play an important role in the hot ends of jet engines and land-based gas turbines. However, high temperature creep which results from the summation of both stress and elemental diffusion is an inevitable failure mode in service. Among many inherent factors, the grain boundary is a crucial one because of its migration at high temperature during creep process. In order to improve the high-temperature creep property, new generations of superalloys have been developed in which grain boundaries are significantly eliminated by means of either directional solidification or single crystal growth [1–5]. Unfortunately, compared with the traditional casting, the efficiency of producing new generation superalloys is lower especially when the desired components are large and the shape geometry is irregular. Therefore, an alternative method with addition of microelements such as carbon (C) and boron (B) for strengthening the grain boundaries is extensively adopted [6–10]. Hence nowadays C/B is added into almost all commercial superalloys. Besides segregations at the grain boundaries or phase boundaries [11–13], the presence of C/B is also known in the form of carbide and boride precipitations [14–20] which greatly dominate the property of the materials. Thus, microstructural details on the precipitations are very fundamental and critical for a better understanding of the relationships between the microstructure and the properties. In contrast to carbides, structural characteristics of borides especially the M_2B-type borides, where M represents transitional metal elements, is known little due to their complicated and usually heavily faulted structure [21–26].

In our previous study, several structural details of the polytypic M_2B phase were observed through the conventional transmission electron microscopy (TEM) [26], such as the stacking fault plane and displacement vector of stacking faults, 60° rotation twin, intergrowth between C16 and C_b structure (C16, C_b for Strukturbericht notations). However, two critical issues still remain unclarified. First, atomic configurations for above mentioned various kinds of planar defects are lacking direct evidence, despite the fact that these are significantly important for the first-principles calculations and large-scale atomistic modeling. Fortunately, benefiting from the development of aberration corrector, resolutions in both TEM and scanning TEM (STEM) modes are reaching the sub-angstrom scale, which provides the possibility of elucidating many important structural problems at an atomic scale [27–36]. Second, the knowledge on the origination of the polytypic feature in M_2B phase is still controversial. Different from Goldfarb's work in which the origination was attributed to the phase transformation among different variants [21], we proposed that the nature of this polytypism lies in the conservation of anti-square prism in our previous study [26]. Nevertheless, these discussions are short of direct

* Corresponding author.
E-mail address: xlma@imr.ac.cn (X.L. Ma).

http://dx.doi.org/10.1016/j.actamat.2015.08.025
1359-6454/

evidence from the viewpoint of elemental distribution. Meanwhile, the energy minimization was not taken into account.

In this work, we investigate the atomic configurations of various structural intergrowths in the polytypic M_2B-type boride by HAADF imaging technique at an atomic scale. Furthermore, on the basis of advanced spectrometry imaging technique and density functional theory (DFT) calculations, we rationalize the polytypic intergrowth frequently observed in the M_2B phase.

2. Experimental procedures

2.1. Bulk sample preparation

The bulk sample used in the present work is a long-term aging heat resistant polycrystalline superalloy with the nominal composition of 15.5 Cr, 10.8 Co, 2.1 Mo, 5.6 W, 3.2 Al, 4.6 Ti, 0.2 Nb, 0.4 Hf, 0.073 C, 0.075 B, and balance Ni, in wt%. The as-cast alloy was firstly solution treated at 1170 °C for 4 h followed by air-cooling. Subsequently, it is subjected to a two-step aged treatments at 1050 °C for 4 h, 850 °C for 16 h followed by air-cooling. Finally, the standard heat treated alloy was exposed at 900 °C for 10000 h and then air-cooled. Initial TEM discs with a diameter of 3 mm were prepared by cutting, grinding, punching and dimpling to a thickness less than 10 μm in the central area. The final ion-milling was carried out in the Gatan precision ion polishing system (PIPS) with a liquid-nitrogen-cooled stage for avoiding preferential thinning effects. The perforated specimen was plasma cleaned in the Advanced Plasma System Gatan Solarus 950 before loading into TEM for eliminating the surface contamination.

2.2. Composition analysis and STEM imaging

The microstructural and chemical investigations were conducted on the aberration corrected Titan^{3TM} G^2 60–300 transmission electron microscope (TEM) operated at 300 kV. The facility is equipped with a high-brightness field-emission gun (X-FEG), double Cs correctors from CEOS, a monochromator and a Gatan Quantum electron energy loss (EEL) spectrometer. In the STEM mode, the convergence semi-angle of electron beam is approximately 25 mrad, which yields a probe size less than 0.10 nm. The collection semi-angle of HAADF detector is in the range of 50–250 mrad. The final resolution approximates 0.08 nm in the HAADF–STEM imaging mode. The processing method of average background subtraction filter (ABSF) was performed on the atomic resolution HAADF images to subtract the noise signal arising from the amorphous layer at the surface of specimen [37]. The Fast Fourier Transformed (FFT) patterns of the atomic resolution images were used to determine the exact projected directions. The energy dispersion employed for EEL spectrometry (EELS) analysis is 0.25 eV per channel. According to the thickness map acquired from energy filtered TEM (EFTEM), the final thickness used for atomic resolution *Z*-contrast imaging and spectrometry imaging analysis ranges from 20 nm to 80 nm.

2.3. Theory calculations

For density functional theory (DFT) calculations, we used the Perdew–Burke–Ernzerhof exchange–correlation function [38] within the generalized gradient approximation and the projector-augmented waves method [39], which is implemented in VASP [40,41]. The energy cutoff was set at 500 eV. A very accurate optimization of structural parameters was achieved by minimizing the forces (below 0.001 eV/A°) and stress tensors (typically below 0.5 kB). The well-converged results used for the Brillouin zone integration of Cr_2B with I4/mcm (C16), Fddd (C_b), $P6_222$ (C_a) and C2/m (N2) structure were obtained by utilizing dense $9 \times 7 \times 7$, $9 \times 9 \times 11$, $7 \times 7 \times 9$ and $7 \times 7 \times 11$ *k*-point grids, respectively.

3. Results and discussion

A review of the available literatures [21,23–26] suggests that M_2B grains are always heavily faulted and exhibit complicated structural features. Thus, any structural analysis only from experimental observations without a rational structural model is usually not convincing enough. Therefore, in order to gain a better understanding of the acquired experimental results, we have to first reveal the structural characteristics of M_2B-type boride in the light of some correlative crystallographic considerations.

3.1. Crystallographic considerations of the polytypic Cr_2B-type boride

According to the published work [23,24,26], M_2B phase precipitated in Ni-based superalloys is mainly composed of elements Cr and B. Thus, we can regard the M_2B-type boride as Cr_2B phase with some other metallic solution elements such as W/Fe in it. In addition, considering the constituted polyhedron of anti-square prism, we have also known that C16-Al_2Cu, C_b-Mg_2Cu and C_a-Mg_2Ni (C_a for Strukturbericht notation) structures are closely related to one another [42]. Therefore, if C16-, C_b-, and C_a-Cr_2B co-exist inside one grain, what will happen deserves further investigation. The space groups, lattice parameters and atomic occupations for the complete C16-, C_b-, and C_a-Cr_2B structures are listed in Table 1. It is seen that the lattice vectors of C16-, C_b-, and C_a-Cr_2B are closely related to each other, as shown intuitively in Fig. 1a. The $[010]_{C_a}$ direction in C_a-Cr_2B is equivalent to $[001]_{C16}$ in C16-Cr_2B and $[001]_{C_b}$ in C_b-Cr_2B. The $[210]_{C_a}$ direction in C_a-Cr_2B is equivalent to $[1\bar{1}0]_{C16}$ in C16-Cr_2B and $[010]_{C_b}$ in C_b-Cr_2B. For the sake of correlation, we herein introduce a basic orthorhombic lattice using the lattice vectors of $\boldsymbol{a_O}$, $\boldsymbol{b_O}$, $\boldsymbol{c_O}$ with the following definitions:

$$\boldsymbol{a_O} = \mathrm{OA} = [001]_{C_a}/3 = [110]_{C16}/2 = [100]_{C_b}/4;$$

$$\boldsymbol{b_O} = \mathrm{OB} = [210]_{C_a} = [1\bar{1}0]_{C16} = [010]_{C_b};$$

$$\boldsymbol{c_O} = \mathrm{OC} = [010]_{C_a} = [001]_{C16} = [001]_{C_b}.$$

Table 1
Structure types, space groups, lattice parameters, Wyckoff positions and fractional atom coordinates for the C16-, C_b- and C_a-Cr_2B phases.

Structure	Space group	Unit cell (nm)	Atom	Fractional coordinates		
Cr_2B	I4/mcm	a = 0.519	Cr (8h)	0.167	0.667	0.000
C16	(No. 140)	c = 0.432	B (4a)	0.000	0.000	0.250
		a = 1.471	Cr (16e)	0.917	0.000	0.000
Cr_2B	Fddd	b = 0.741	Cr (16f)	0.000	0.333	0.000
C_b	(No. 70)	c = 0.425	B (16e)	0.373	0.000	0.000
		a = 0.423	Cr (6f)	0.500	0.000	0.390
Cr_2B*	$P6_222$	c = 1.095	Cr (6j)	0.166	0.332	0.500
C_a	(No. 180)	β = 120°	B (3a)	0.000	0.000	0.333
			B (3c)	0.500	0.500	0.333

* Structural information for the C_a-Cr_2B phase was determined recently in our previous work [26].

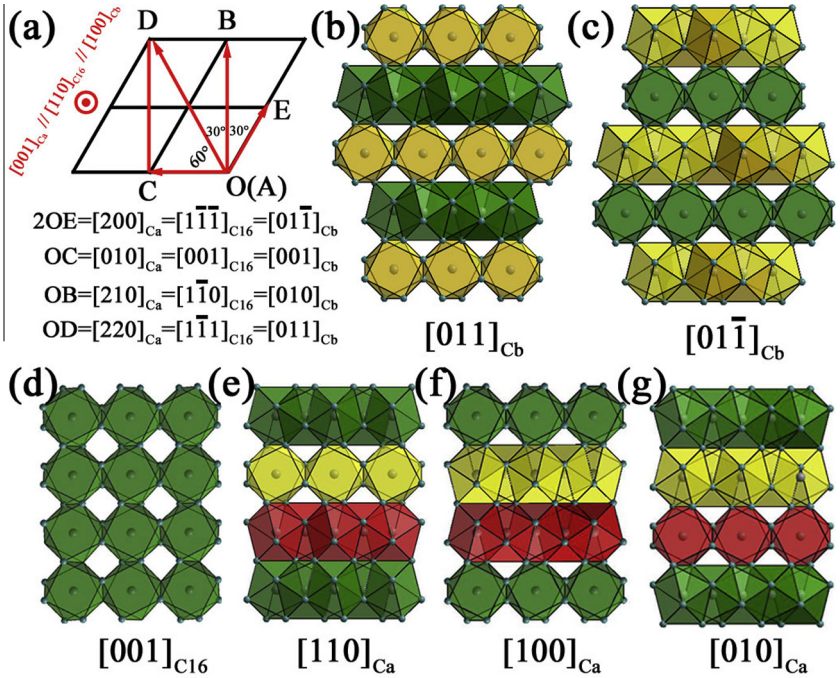

Fig. 1. (a) A schematic diagram showing the directional equivalence among C16-, C_b-, and C_a-Cr_2B in the conjunct planes of $(110)_{C16}$, $(100)_{C_b}$ and $(001)_{C_a}$. The structural projections of orthorhombic C_b-M_2B along (b) $[011]_{C_b}$ and (c) $[01\bar{1}]_{C_b}$ directions; tetragonal C16-Cr_2B along (d) $[001]_{C16}$ direction; and hexagonal C_a-Cr_2B along (e) $[110]_{C_a}$, (f) $[100]_{C_a}$ and (g) $[010]C_a$ directions displaying the polyhedral configurations in each structure. The shaded red, green and yellow polyhedrons represent three sets of anti-square prisms with their 4-fold axes along different directions. The polyhedron of single anti-square prism is comprised of eight Cr atoms at the vertexes and one B atom at the center. (For interpretation of the references to color in this figure legend, the reader is referred to the web version of this article.)

Here the subscript ***O*** represents the basic orthorhombic lattice. Consequently, we find that the $2\boldsymbol{c_O}$ ($[020]_{C_a}$, $[002]_{C16}$, $[002]_{C_b}$) direction is also equivalent to $\boldsymbol{b_O}+\boldsymbol{c_O}$ ($[220]_{C_a}$, $[1\bar{1}1]_{C16}$, $[011]_{C_b}$) and $\boldsymbol{b_O}-\boldsymbol{c_O}$ ($[200]_{C_a}$, $[1\bar{1}\bar{1}]_{C16}$, $[01\bar{1}]_{C_b}$) directions. Moreover, the intersection angle between $\boldsymbol{c_O}$ and $\boldsymbol{b_O}+\boldsymbol{c_O}$ is 60°, which is the same as the angle between $\boldsymbol{b_O}+\boldsymbol{c_O}$ and $\boldsymbol{b_O}-\boldsymbol{c_O}$. On the basis of this unified orthorhombic lattice, we define the lattice length of $\boldsymbol{a_O}$ as one lattice period. Then, the intrinsic structural difference among C16-, C_b-, and C_a-Cr_2B only rests with the variation of period number along $\boldsymbol{a_O}$ direction. To be more specific, for Cr_2B boride with C16, C_a and C_b structures, the period number n equals to 2, 3 and 4, respectively.

In order to unveil the inherent relationships of the three variants mentioned above, structural projections along some important crystallographic orientations are given and displayed in Fig. 1b–g, where the polyhedron units of anti-square prisms marked by red, yellow and green color represent the polyhedra with different 4-fold directions. It is seen that the C16-Cr_2B structure contains only one set of anti-square prim with its 4-fold direction along $[001]_{C16}$, namely the $\boldsymbol{c_O}$ direction, as shown in Fig. 1d. While for C_b-Cr_2B, it consists of two sets of anti-square prims with their 4-fold directions along $[011]_{C_b}$ and $[01\bar{1}]_{C_b}$, namely the $\boldsymbol{b_O}+\boldsymbol{c_O}$ and $\boldsymbol{b_O}-\boldsymbol{c_O}$ directions, as shown in Fig. 1b and c, respectively. As for C_a-Cr_2B, it contains three sets of anti-square prims with their 4-fold directions along $[110]_{C_a}$, $[100]_{C_a}$ and $[010]_{C_a}$, namely the $\boldsymbol{b_O}+\boldsymbol{c_O}$, $\boldsymbol{b_O}-\boldsymbol{c_O}$ and $\boldsymbol{c_O}$ directions, as shown in Fig. 1e–g, respectively. Now it is apparent that the close relationships among C16-, C_b-, and C_a-Cr_2B actually originate from the polyhedral configuration of anti-square prism which is comprised of eight Cr atoms at the vertexes and one B atom at the center. Thus, the locations of B atoms are definitively determined once Cr atoms are fixed. Moreover, it is worthwhile to mention that the B atoms in M_2B lattice are invisible in the atomic resolution TEM/HAADF images because of their weak scattering ability compared with that of transitional metal atoms represented by M. Therefore, we can only consider the skeleton of Cr atoms for a simplified description.

Fig. 2a is a structural projection of C_a-Cr_2B along $[100]_{C_a}$ direction, in which we introduce four closely related structural units named as A, <u>A</u>, B and <u>B</u> as shown in the upper left part. Compared with the structural unit A, structural units B, <u>A</u> and <u>B</u> have a $[100]_{C_a}/4$, $[100]_{C_a}/2$, 3 $[100]_{C_a}/4$ displacement along the projection direction, respectively. Based on above closely related structural units, the projection of C_a-Cr_2B along $[100]_{C_a}$ orientation can be simplified, as shown in Fig. 2b. Moreover, we infer that the fractional atomic coordinates along $[1\bar{1}1]_{C16}$ and $[011]_{C_b}$ projected directions can be given based on $[1\bar{1}1]_{C16}/2$ and $[011]_{C_b}/2$, because the $(\boldsymbol{b_O}+\boldsymbol{c_O})/\boldsymbol{2}$ orientation, namely $[1\bar{1}1]_{C16}/2$, $[011]_{C_b}/2$ and $[110]_{C_a}$ directions, is not only the translation period of respective lattice but also equivalent to $\boldsymbol{c_O}$, namely $[001]_{C16/C_b}$ and $[010]_{C_a}$ directions as stated above. Therefore, it is reasonable to adopt the structural units introduced through C_a lattice to simplify the projections of C16 and C_b structures along $[001]_{C16}$, $[1\bar{1}1]_{C16}$, $[001]_{C_b}$ and $[011]_{C_b}$ directions, as shown correspondingly in Fig. 2c–f. In consideration of the similarity among structural projections simplified above, we deduce that there may be various types of intergrowth in the grains. Particularly, if $[001]_{C16}$ ($[001]_{C_b}$) and $[1\bar{1}1]_{C16}$ ($[011]_{C_b}$) coexist in one grain, we can name it as 60° rotation twin in C16 (C_b) structure with the rotation axis along $[110]_{C16}$ ($[100]_{C_b}$) direction; if $[001]_{C16}$ ($[1\bar{1}1]_{C16}$) and $[001]_{C_b}$ ($[011]_{C_b}$) coexist in one grain, we name it as the normal intergrowth between C16 and C_b variants; if $[001]_{C16}$ ($[1\bar{1}1]_{C16}$)

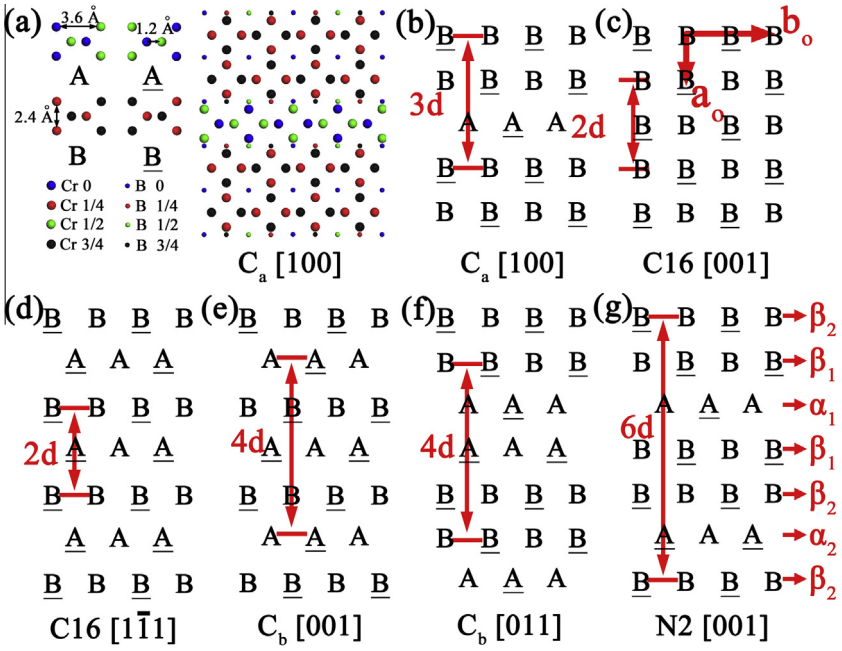

Fig. 2. (a) Structural projection along $[100]_{C_a}$ orientation of C_a-Cr_2B and (b) the corresponding simplified description showing the configurations of the basic structural units A, A, B and B. The fractional atom coordinates along the projected direction and the distances among different atomic columns for the basic structural units are indicated. (c–g) Structural simplification of $[001]_{C16}$, $[1\bar{1}1]_{C16}$, $[001]_{C_b}$, $[011]_{C_b}$ and $[001]_{N2}$ directions, respectively, displaying the inherent relationship among above projected directions. The fractional atom coordinates along projection directions in (d) and (f) are given based on $[1\bar{1}1]_{C16}/2$ and $[011]_{C_b}/2$, respectively. The indicated $\boldsymbol{a_O}$ and $\boldsymbol{b_O}$ directions in (c) are based on the basic unified orthorhombic lattice. The denoted 2*d*, 3*d*, 4*d* and 6*d* represent the periodicity along the stacking direction of $\boldsymbol{a_O}$ for C16-, C_b-, C_a-, and N2-Cr_2B structures respectively, in which *d* is the lattice length of $\boldsymbol{a_O}$. The denoted layers α_1, α_2, β_1 and β_2 in (g) represent four different stacking layers.

and $[011]_{C_b}$ ($[001]_{C_b}$) coexist in one grain, we name it as the twin-related intergrowth between C16 and C_b, which results from the 60° rotation twin of C16/C_b variants.

Furthermore, here it is worthwhile to mention that the structural projections along $[1\bar{1}1]_{C16}$ and $[001]_{C_b}$ directions (Fig. 2d and e) are very similar. The minor difference only lies in the fractional atom coordinates along the projected directions. This indicates that it is impossible to distinguish these two simply from the experimental atomic resolution TEM/HAADF images due to the loss of height information along the incident direction. Thereby, according to the atomic resolution images, the normal intergrowth between C16 and C_b is indistinguishable from the 60° rotation twin in C16/C_b structures. The only way to distinguish them is via large-angle tilting technique to orientate the grain to another zone-axis, as elucidated in our previous work [26]. However, in the present work, we do not intend to put our efforts on distinguishing these two directions because it is difficult to differentiate one particular area from its neighboring region along different zone-axes in the high resolution mode. Furthermore, based on the stacking characteristics parallel to $[100]_{C_a}$, $[001]_{C16}$, $[1\bar{1}1]_{C16}$, $[001]_{C_b}$ and $[011]_{C_b}$ axes (Fig. 2b–f), we can speculate a new structural variant named N2 (for keeping uniformity with the previous work [26]) with the simplified description deduced according to the basic orthorhombic lattice, as shown in Fig. 2g. Now, it is noted that the structural characteristics along $[100]_{C_a}$ (Fig. 2b) and $[001]_{N2}$ (Fig. 2g) projections are also indistinguishable from the experimental atomic resolution images because of the loss of height information along the incident direction, which is analogous to the situation in $[1\bar{1}1]_{C16}$ and $[001]_{C_b}$ projections. In Fig. 2b–g, the lattice periods of 2*d*, 3*d*, 4*d* and 6*d* for various variants along the stacking direction $\boldsymbol{a_O}$ are indicated, where *d* is the length of $\boldsymbol{a_O}$ vector.

In view of simplified descriptions displayed in Fig. 2b–g, we can further reveal the configuration rule for the basic structural units (A, A, B and B) and propose a more general model to depict the Cr_2B polytypism. Hereon, we define the layers beginning with A, A, B, B as α_1, α_2, β_1, β_2 as shown in Fig. 2g. It is obvious that the structural units A (B) and A (B) arrange alternatively along $\boldsymbol{b_O}$ direction in each layer for various variants. Along the stacking direction $\boldsymbol{a_O}$, the layer next to α_1 (α_2) layer can be α_2 (α_1), β_1 (β_2) or β_2 (β_1) layer; the layer next to β_1 (β_2) layer can be β_2 (β_1), α_1 (α_2) or α_2 (α_1) layer. Specially, the β layer should have a displacement of $\boldsymbol{b_O/4}$ along the $\boldsymbol{b_O}$ direction if the β (including β_1

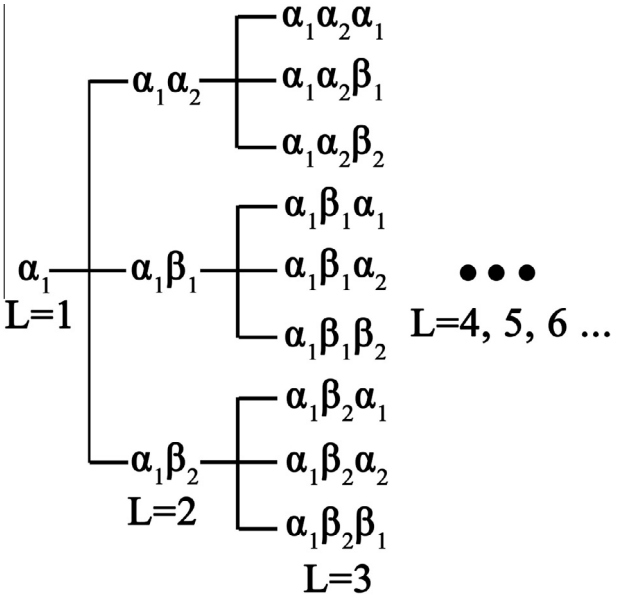

Fig. 3. A schematic of structural derivations displaying the layer arrangement along the $\boldsymbol{a_O}$ direction for polytypic Cr_2B phases with any number of stacking layers. The *L* represents the number of stacking layer along $\boldsymbol{a_O}$ direction.

and β_2) layer is after α (including α_1 and α_2) layer; the α layer should also have a displacement of $\boldsymbol{b_O/4}$ along the $\boldsymbol{b_O}$ direction if the α layer is after β layer. Consequently, the layer arrangements for C16, C_b and C_a variants along some equivalent directions, such as $[001]_{C16}$, $[1\bar{1}1]_{C16}$, $[001]_{C_b}$, $[011]_{C_b}$ and $[100]_{C_a}$ can be simply denoted as $\alpha_1\alpha_2\alpha_1$ ($\beta_1\beta_2\beta_1$), $\alpha_1\beta_{1/2}\alpha_1$ ($\beta_1\alpha_{1/2}\beta_1$), $\alpha_1\beta_{1/2}\alpha_2\beta_{2/1}\alpha_1$ ($\beta_1\alpha_{1/2}\beta_2\alpha_{2/1}\beta_1$), $\alpha_1\alpha_2\beta_{1/2}\beta_{2/1}\alpha_1$ ($\beta_1\beta_2\alpha_{1/2}\alpha_{2/1}\beta_1$), and $\alpha_1\beta_{1/2}\beta_{2/1}\alpha_1$ ($\beta_1\alpha_{1/2}\alpha_{2/1}\beta_1$), respectively. Moreover, taking into account of above configuration rules for the layers α_1, α_2, β_1 and β_2, we can easily label the structures of the polytypic Cr_2B containing any number of stacking layers, as shown in Fig. 3, irrespective of the specific stacking periods or structural variants.

3.2. Microstructural and chemical observation of M_2B-type boride

Fig. 4a is a low-magnification HAADF–STEM image obtained from the area including both the M_2B and the matrix along the $[001]_{C16}$ orientation. M_2B grain exhibits dark contrast, suggesting a low average atomic number (Z) compared with that of the matrix. To display the structural characteristics at a micro-scale, electron diffraction patterns (EDPs) were acquired from the area I, II and III indicated in Fig. 4a and shown in Fig. 4b–d, respectively. Regardless of the intense streaking effect, the EDPs of Fig. 4b–d can be indexed as $[001]_{C16}//[1\bar{1}1]_{C16}//[001]_{C_b}//[011]_{C_b}$. The obvious variation of EDPs in Fig. 4b–d implies the structural inhomogeneity inside M_2B grain, as evidenced by the atomic resolution HAADF images shown in Fig. 5a–c, which were obtained approximately from the area I, II and III marked in Fig. 4a, respectively. Close attention should be paid here to note that Fig. 5a–c have a 90° plane rotation relative to Fig. 4a.

The contrast difference inside M_2B grain marked by an arrow in Fig. 4a deserves our close attention. It is widely accepted that the HAADF–STEM technique provides atomic number (Z) contrast with

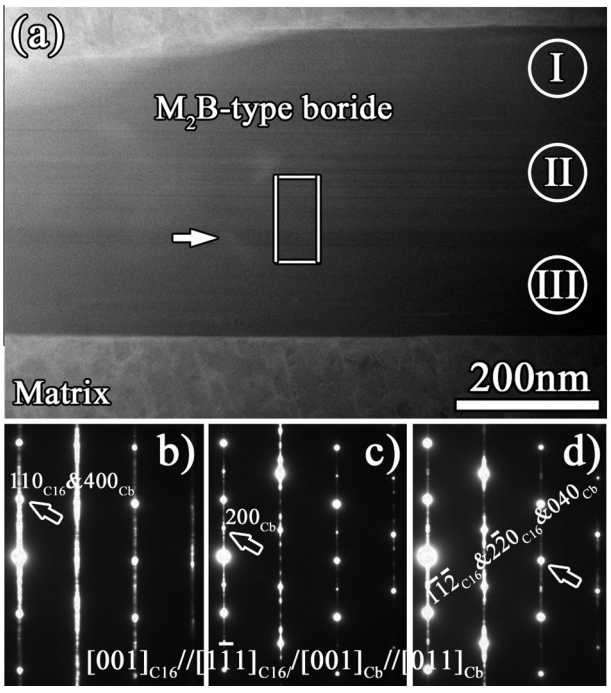

Fig. 4. (a) Low magnification HAADF–STEM image showing the structural inhomogeneity inside the M_2B grain precipitated in the matrix. The arrow indicates the inhomogeneous contrast inside M_2B grain. The rectangle frame represents the area used for EEL spectrometry (EELS) image scan. (b–d) Partial EDPs corresponding to area I, II, and III indicated in (a), respectively, can be recorded along $[001]_{C16}//[1\bar{1}1]_{C16}//[001]_{C_b}//[011]_{C_b}$ zone-axis.

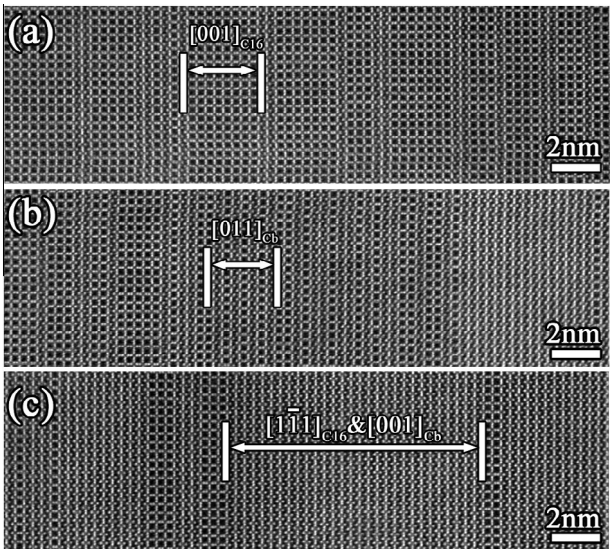

Fig. 5. (a–c) Atomic resolution HAADF images obtained from regions I, II, III (indicated in Fig. 4a) respectively displaying the structural inhomogeneity inside M_2B grain. Based on the experimental atomic resolution images, the $[001]_{C_b}$ and $[1\bar{1}1]_{C16}$ orientations denoted in (c) are indistinguishable due to the loss of height information along the incident direction.

the intensity in proportion to $Z^{1.7-1.9}$ [43–45]. Thereby, the contrast inhomogeneity inside this M_2B grain may be related with compositional variations. In order to reveal the chemical information, EELS technique was utilized. EELS profile shown in Fig. 6a displays the main chemical elements in M_2B phase. The minor W element as evidenced by energy dispersive spectrometry (EDX) analysis in our previous work [26] was not detected here because of its high core loss peak. In addition, it is noticeable that there is no detectable carbon in the M_2B grain although the contents of C and B in our alloy are almost the same. Therefore, the M_2B phase precipitated in the present alloy is indeed boride not car-boride as discussed in others' work [25]. Furthermore, the advanced spectrometry imaging technique was performed on the rectangle area indicated in Fig. 4a for the sake of specifying the elemental distribution inside M_2B grain. The detailed results are displayed in Fig. 6b–d. The real-time image shown in Fig. 6b indicates that there is no spatial drift. The elemental maps imaged by B–K and Cr-$L_{2,3}$ core loss peak demonstrate that there is no elemental variations inside the M_2B grain. Similarly, the chemical homogeneity is again confirmed through the EELS line-scan across the matrix and M_2B grain as shown in Fig. 6e. These chemical analyses suggest that the contrast difference inside M_2B grains should not result from the elemental variations. In other aspects, although the elastic fields in the specimen can also modify the contrast in the HAADF–STEM mode in a complex manner [46–48], the contrast difference inside M_2B grains should not arise from strains because there is no lattice distortion in the polytypic M_2B structure as evidenced by former crystallographic considerations. Interestingly, by carefully checking the microstructure of M_2B grain, we find that the area with dark contrast exhibits the structural characteristic of C16 along $[001]_{C16}$ direction, as indicated in Fig. 5a. Therefore, considering the holes for the anti-square prisms along their 4-fold directions, we suppose that the contrast difference inside the M_2B grain may originate from the channeling effect.

3.3. Atomic imaging of various kinds of intergrowth in M_2B-type boride

Upon former crystallographic considerations, we propose that various kinds of structural intergrowth may coexist inside M_2B

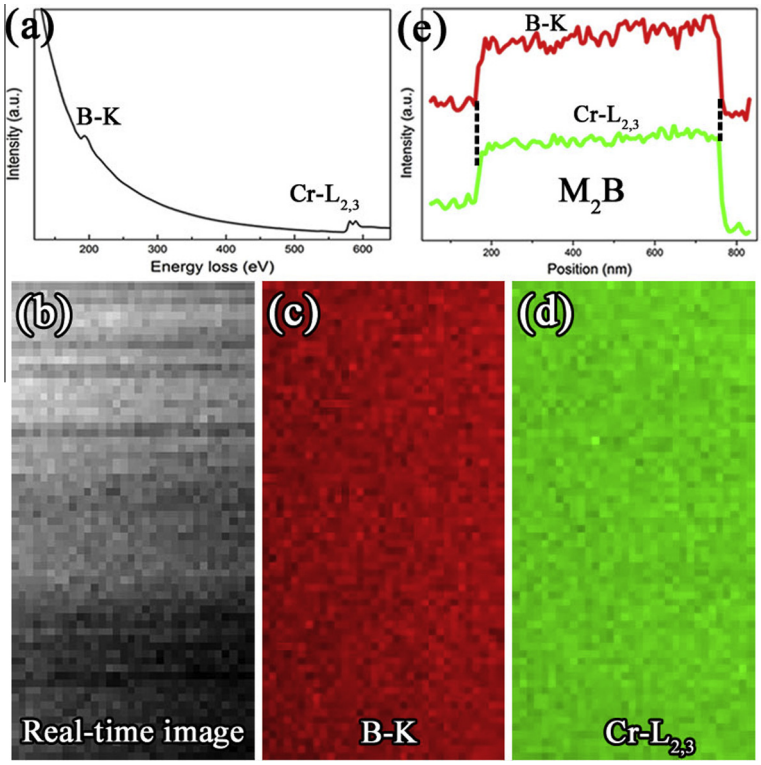

Fig. 6. (a) EELS profile displaying the primary elements in M_2B phase. (b–d) EELS elemental mapping images of the rectangle framed zone (indicated in Fig. 4a) corresponding to (b) real-time image, (c) B–K, (d) Cr–$L_{2,3}$ map, displaying the chemical homogeneity inside M_2B grain. (e) EELS line scan across the M_2B boride and matrix again showing the chemical homogeneity inside M_2B grains.

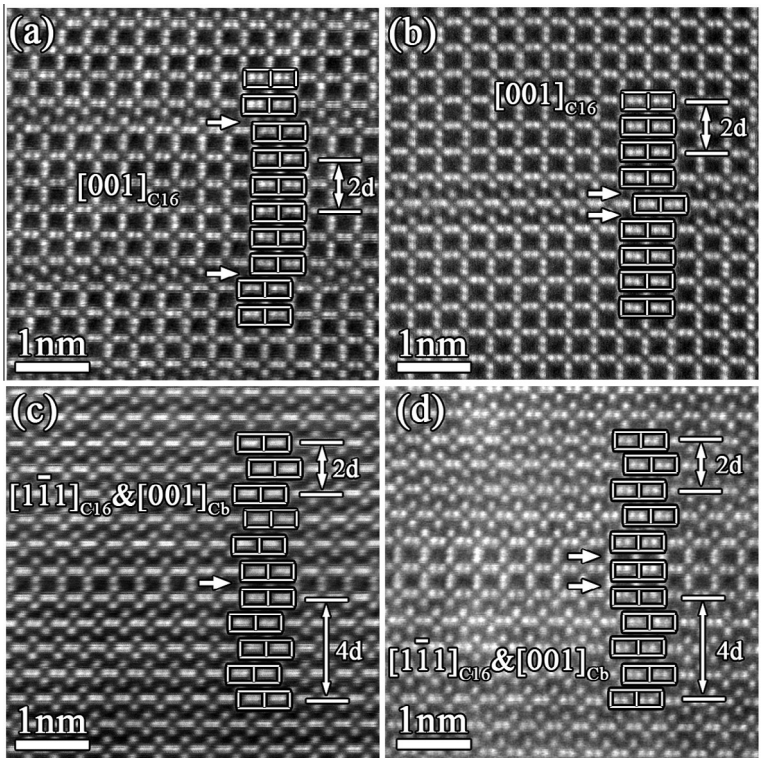

Fig. 7. Atomic resolution HAADF images displaying (a) two separated, (b) two consecutive stacking faults in C16 structure incident along $[001]_{C16}$ direction; and (c) one, (d) two consecutive stacking faults in C_b structure incident along $[001]_{C_b}$ direction or in C16 structure incident along $[1\bar{1}1]_{C16}$ direction. According to the experimental atomic resolution images, the $[001]_{C_b}$ and $[1\bar{1}1]_{C16}$ orientations denoted in (c) and (d) are indistinguishable due to the loss of height information along the incident direction. The symbols 2*d* and 4*d* represent the periodicity along the stacking direction $\boldsymbol{a_O}$ for C16- and C_b-Cr_2B structures respectively, in which *d* is the lattice length of $\boldsymbol{a_O}$.

grain. In order to demonstrate these structural details, atomic resolution HAADF images were obtained from the heavily faulted M_2B grain. Fig. 7a is an atomic resolution HAADF image projected along $[001]_{C16}$ direction, indicating that there are two separated stacking faults in C16 structure. And the layer arrangement along the stacking direction $\boldsymbol{a_O}$ for C16 with single fault can be labeled as $\alpha_1\alpha_2\alpha_1\beta_1\beta_2\beta_1$ or $\alpha_1\alpha_2\alpha_1\beta_2\beta_1\beta_2$. It is worthy to point out here that there may be several denotations for the layer arrangement even for a simply faulted structure. Thus, in the following structural analyses, we will give only one marking form for simplification. In Fig. 7b, we can deem that there are two consecutive stacking faults in the C16 lattice with the layer arrangement labeled as $\alpha_1\alpha_2\alpha_1\beta_2\alpha_1\alpha_2$, in which a unit cell of the C16 structure along $[1\bar{1}1]_{C16}$ direction is generated with the stacking layers of $\alpha_1\beta_2\alpha_1$. Correspondingly, there can also be single or consecutive two stacking faults in C_b structures, as shown in Fig. 7c and d, respectively. Fig. 7c shows that the layer arrangement of the faulted structure contains single stacking fault, which can be labeled as $\alpha_1\beta_2\alpha_2\beta_1\alpha_1\alpha_2\beta_1\alpha_2$. It is seen that the structural fragments of C_a along $[100]_{C_a}$ direction are generated with the stacking layers of $\beta_1\alpha_1\alpha_2\beta_1$ and $\alpha_2\beta_1\alpha_1\alpha_2$. Fig. 7d displays the faulted structure which contains two consecutive stacking faults and can be labeled as $\alpha_1\beta_2\alpha_2\beta_1\alpha_1\alpha_2\alpha_1\beta_2\alpha_2$, where a unit cell of C16 structure along $[001]_{C16}$ direction is generated with the layer arrangement of $\alpha_1\alpha_2\alpha_1$. Considering that the structural characteristics in $[001]_{C_b}$ and $[1\bar{1}1]_{C16}$ directions are undistinguishable from the experimental atomic resolution images, we realize that the atomic resolution HAADF images (Fig. 7c and d) can also be obtained parallel to $[1\bar{1}1]_{C16}$ orientation. If single stacking fault is introduced in $[1\bar{1}1]_{C16}$ projection (Fig. 7c), the layer arrangement can be labeled as $\alpha_1\beta_2\alpha_1\alpha_2\beta_1\alpha_2$, in which the stacking sequence along $[1\bar{1}1]_{C16}$ changes from $\alpha_1\beta_2\alpha_1$ to $\alpha_2\beta_1\alpha_2$. However, this newly formed structural characteristic ($\alpha_2\beta_1\alpha_2$) along $[1\bar{1}1]_{C16}$ direction and the primitive structural characteristic ($\alpha_1\beta_2\alpha_1$) are undistinguishable due to the loss of height information along the incident direction. If two consecutive stacking faults are introduced in $[1\bar{1}1]_{C16}$ projection (Fig. 7d), the layer arrangement can be labeled as $\alpha_1\beta_2\alpha_1\alpha_2\alpha_1\beta_2\alpha_1$, in which a unit cell of C16 structure along $[001]_{C16}$ direction is generated with the layer arrangement of $\alpha_1\alpha_2\alpha_1$.

Besides the unit-cell scale intergrowths caused by single or two consecutive stacking faults, large-scale coexistence among C16, C_b and C_a are also observed in our experiment, as shown in Fig. 8a–d. In Fig. 8a, the upper and lower parts display the normal intergrowth between C16 and C_b structure, because they can be obtained along both $[001]_{C16}$ and $[001]_{C_b}$ directions. Meanwhile, in consideration of the indistinguishability between the structures along $[001]_{C_b}$ and $[1\bar{1}1]_{C16}$ projections from the experimental images as stated above, we can also regard Fig. 8a as the 60° rotation twin in C16 structures with the rotation axis along $[110]_{C16}$. Similarly, Fig. 8b can either display the normal intergrowth between C16 and C_b along $[1\bar{1}1]_{C16}$ and $[011]_{C_b}$ or imply the 60° rotation twin in C_b with the rotation axis along $[100]_{C_b}$. In contrast, Fig. 8c reveals the twin-related intergrowth between C16 and C_b structures because the upper and lower areas can be recorded along $[001]_{C16}$ and $[011]_{C_b}$, respectively. As for Fig. 8d, it demonstrates the intergrowth between C16 and C_a/N2 lattices, since the upper and lower microstructures can be obtained along $[001]_{C16}$ and $[100]_{C_a}/[001]_{N2}$, respectively. This observation agrees well with our crystallographic considerations discussed in the previous

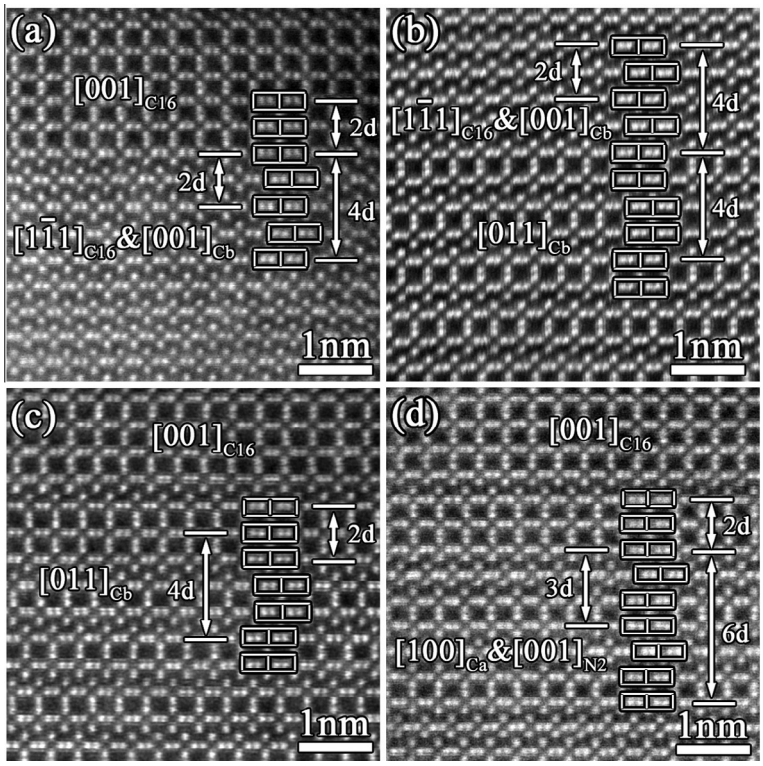

Fig. 8. Atomic resolution HAADF images displaying various kinds of large-scale structural intergrowth. Note that the atomic resolution HAADF images along $[1\bar{1}1]_{C16}$ and $[001]_{C_b}$ are indistinguishable. So if the lower part of (a) and upper part of (b) are labeled as $[1\bar{1}1]_{C16}$ and $[001]_{C_b}$, respectively, atomic resolution images of (a) and (b) will reveal the 60° rotation twin in C16 and C_b structures, respectively; while if the lower part of (a) and upper part of (b) are labeled as $[001]_{C_b}$ and $[1\bar{1}1]_{C16}$, respectively, atomic resolution images of (a) and (b) reveals the normal intergrowth between C16 and C_b structures. (c) twin-related intergrowth between C16 and C_b; and (d) intergrowth between C16 and C_a/N2. The denotation 2*d*, 3*d*, 4*d* and 6*d* represent the periodicity along the stacking direction $\boldsymbol{a_O}$ for C16-, C_b-, C_a-, and N2-Cr_2B structures, respectively.

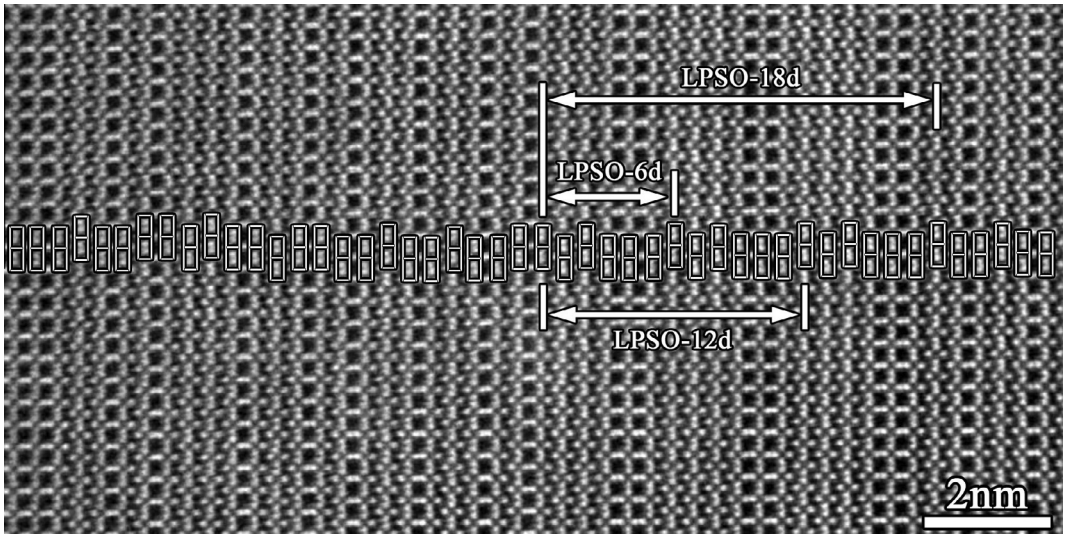

Fig. 9. Atomic resolution HAADF image along $[001]_{C16}$ direction displaying the long period stacking order (LPSO) structure with the uncertain period number of 6, 12, 18 or even bigger.

section. Moreover, we have also captured the structural variants with a large period number along $\boldsymbol{a_O}$ direction, namely the long period stacking order (LPSO) structure, as shown in Fig. 9. As for its specific period number n, it can be 6, 12, 18 or even bigger. It is hard to determine the specific period from the experimental image owing to the loss of height information along the incident beam direction. As a matter of fact, for the LPSO structure, we could also regard it as an ordered intergrowth among three basic structures (C16, C_b and C_a) along some equivalent crystallographic directions, such as $[001]_{C16}$, $[1\bar{1}1]_{C16}$, $[001]_{C_b}$, $[011]_{C_b}$ and $[100]_{C_a}$.

3.4. Energy consideration for the polytypic characteristics of M_2B phase

As for the nature of the polytypic characteristics of M_2B phase, it is still an open question. In Goldfarb's work [21], the polytypic characteristic of M_2B boride that precipitated in the alloyed steel was attributed to the stacking faults, which resulted from the phase transformation between C16-$(Fe, Cr)_2B$ and C_b-$(Cr, Fe)_2B$ due to the elemental segregation inside M_2B grain. However, the critical proof of elemental variations that supports this opinion was not given. In regard of the M_2B borides precipitated in the present alloy, the elemental distribution inside single grain is homogeneous as shown in Fig. 6b–e. Furthermore, this phenomenon is also reproducible in our alloy. Therefore, we believe that the intrinsic reason for the polytypic feature is the structural characteristics, namely the conservation of basic anti-square prism which constitutes the M_2B phase, other than phase transformations.

Additionally, besides the composition analysis, we have also sought out more solid evidence by means of some correlative considerations from the energy minimization. Fig. 10 compares the energy differences of Cr_2B borides with the various structures from DFT calculations. It is seen that the energy variations of C16, C_b and C_a are nearly the same. Even for the N2 variant with a large periodicity, the energy difference is also negligible. Considering that the general feature of various variants is the conservation of basic anti-square prism, we can conclude that any structural characteristics including stacking faults and intergrowths possess a low-energy state because the basic polyhedron of anti-square prism remains undestroyed. And the conservation of the basic polyhedrons can be ensured by complying with the configuration rule for the layers of α_1, α_2, β_1 and β_2 along $\boldsymbol{a_O}$ direction.

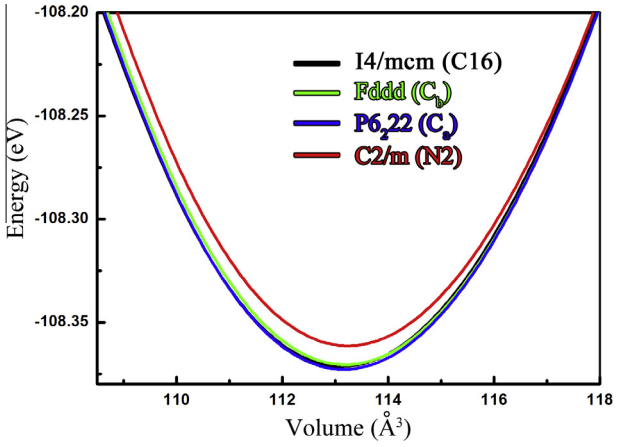

Fig. 10. Theoretical calculations of energy vs volume curves displaying the relative stability of Cr_2B borides with four different structural variants, namely, C16, C_b, C_a and N2. The N2 is given based on the basic orthorhombic lattice and its true space group is C2/m.

4. Conclusions

The profoundly faulted M_2B-type borides precipitated in a long-term aging Ni-based superalloy have been investigated in detail by using the state-of-the-art TEM and further evaluated by DFT calculations. We summarize these observations as follows:

(1) On the basis of detailed crystallographic considerations, the inherent structural characteristics of the polytypic M_2B-type boride are displayed by means of the simplified models. With the state-of-the-art TEM, we demonstrate the atomic configurations of the unit-cell scale intergrowth introduced by one or two consecutive stacking faults in the perfect lattice, and of various kinds of large-scale intergrowth among the basic structural variants, namely C16-, C_b-, and C_a-M_2B. Additionally, we also display the LPSO structure in M_2B grains though it is hard to exclusively determine the specific period number by the experimental atomic resolution image due to the loss of height information along the projected direction.

(2) The nature of polytypic feature of M_2B lies in the conservation of the basic polyhedron of anti-square prism, which is comprised of eight metal atoms at the vertexes and one boron atom at the center. In other words, although various structural variants and the relevant planar faults coexist in single grain, the basic polyhedra remain unchanged. Elemental mappings derived from the advanced spectrometry imaging technique suggest that the chemical inhomogeneity does not occur inside the M_2B grains, implying that the structural inhomogeneity is not associated with the phase transformation.

Acknowledgements

This work is supported by the National Natural Foundation of China (No. 11327901) and Ministry of Science & Technology of China (2010CB631206 and 2009CB623705). We are grateful to Mr. J. Wang for bulk sample preparation, to Mr. B. Wu and Mr. L. X. Yang for technical support at Titan platform, and to Dr. Y.L. Tang and Dr. Z.B. Yu for useful discussions.

References

[1] J.X. Zhang et al., Acta Mater. 53 (2005) 4623.
[2] T.M. Pollock, S. Tin, J. Propul. Power 22 (2006) 361.
[3] R.C. Reed (Ed.), The Superalloys: Fundamentals and Applications, Cambridge University Press, Cambridge, 2006.
[4] S. Ma, L. Carroll, T.M. Pollock, Acta Mater. 55 (2007) 5802.
[5] V.A. Vorontsov et al., Acta Mater. 60 (2012) 4866.
[6] L.R. Liu et al., Mater. Sci. Eng. A 385 (2004) 105.
[7] L. Xiao, D.L. Chen, M.C. Chaturvedi, Metall. Mater. Trans. A 35A (2004) 3477.
[8] L.Z. He et al., Mater. Sci. Eng. A 397 (2005) 297.
[9] L. Xiao, D.L. Chen, M.C. Chaturvedi, Mater. Sci. Eng. A 437 (2006) 157.
[10] B.C. Yan, J. Zhang, L.H. Lou, Mater. Sci. Eng. A 474 (2008) 39.
[11] D.H. Ping et al., Mater. Sci. Eng. A 456 (2007) 99.
[12] D. Tytko et al., Acta Mater. 60 (2012) 1731.
[13] T. Alam et al., Metall. Mater. Trans. A 43A (2012) 2183.
[14] E. Cadel et al., Acta Mater. 50 (2002) 957.
[15] D. Mukherji et al., Scripta Mater. 66 (2012) 60.
[16] J. Wang et al., Mater. Sci. Eng. A 553 (2012) 14.
[17] X.Z. Qin et al., Mater. Sci. Eng. A 543 (2012) 121.
[18] X.B. Hu et al., J. Alloy. Compd. 611 (2014) 104.
[19] X.B. Hu et al., Philos. Mag. Lett. 95 (2015) 237.
[20] N. Sheng et al., Metall. Mater. Trans. A 46A (2015) 1670.
[21] I. Goldfarb et al., Philos. Mag. A 72 (1995) 963.
[22] F.X. Kayser, G.F. Kayser, J. Mater. Sci. 34 (1999) 1271.
[23] M.J. Kaufman, V.I. Levit, Philos. Mag. Lett. 88 (2008) 259.
[24] H.R. Zhang, O.A. Ojo, Philos. Mag. 90 (2010) 765.
[25] S. Ma et al., Acta Mater. 60 (2012) 831.
[26] X.B. Hu, Y.L. Zhu, X.L. Ma, Acta Mater. 68 (2014) 70.
[27] R. Srinivasan et al., Phys. Rev. Lett. 102 (2009) 086101.
[28] M. Huang et al., Acta Mater. 76 (2014) 294.
[29] L. Bourgeois et al., Acta Mater. 59 (2011) 7043.
[30] J.M. Rosalie, C. Dwyer, L. Bourgeois, Acta Mater. 69 (2014) 224.
[31] T. Saito et al., Acta Mater. 78 (2014) 245.
[32] S. Wenner et al., Scripta Mater. 74 (2014) 92.
[33] A. Hirata et al., Nat. Mater. 10 (2011) 922.
[34] J.F. Nie et al., Science 340 (2013) 957.
[35] M. Bugnet et al., Acta Mater. 79 (2014) 66.
[36] X.B. Hu et al., Sci. Rep. 4 (2014) 7367.
[37] R. Kilaas, J. Microsc. 190 (1998) 45.
[38] J.P. Perdew, K. Burke, M. Ernzerhof, Phys. Rev. Lett. 77 (1996) 3865.
[39] P.E. Blochl, Phys. Rev. B 50 (1994) 17953.
[40] G. Kresse, J. Hafner, Phys. Rev. B 47 (1993) 558.
[41] G. Kresse, J. Furthmuller, Phys. Rev. B 54 (1996) 11169.
[42] F. Gingl, P. Selvam, K. Yvon, Acta Crystallogr. B 49 (1993) 201.
[43] S.J. Pennycook, D.E. Jesson, Phys. Rev. Lett. 64 (1990) 938.
[44] P.D. Nellist, S.J. Pennycook, Adv. Imag. Elect. Phys. 113 (2000) 147.
[45] S.J. Pennycook, Adv. Imag. Elect. Phys. 123 (2002) 173.
[46] D.D. Perovic, C.J. Rossouw, A. Howie, Ultramicroscopy 52 (1993) 353.
[47] Z.H. Yu, D.A. Muller, J. Silcox, J. Appl. Phys. 95 (2004) 3362.
[48] V. Grillo, Ultramicroscopy 109 (2009) 1453.